How to cite: *Angew. Chem. Int. Ed.* **2023**, *62*, e202310121
doi.org/10.1002/anie.202310121

Reactive Intermediates | Hot Paper

On-Surface Synthesis and Real-Space Visualization of Aromatic P_3N_3

Qigang Zhong[+], Artur Mardyukov[+], Ephrath Solel[+], Daniel Ebeling, André Schirmeisen, and Peter R. Schreiner**

Abstract: On-surface synthesis is at the verge of emerging as the method of choice for the generation and visualization of unstable or unconventional molecules, which could not be obtained via traditional synthetic methods. A case in point is the on-surface synthesis of the structurally elusive cyclotriphosphazene (P_3N_3), an inorganic aromatic analogue of benzene. Here, we report the preparation of this fleetingly existing species on Cu(111) and Au(111) surfaces at 5.2 K through molecular manipulation with unprecedented precision, i.e., voltage pulse-induced sextuple dechlorination of an ultra-small (about 6 Å) hexachlorophosphazene $P_3N_3Cl_6$ precursor by the tip of a scanning probe microscope. Real-space atomic-level imaging of cyclotriphosphazene reveals its planar D_{3h}-symmetric ring structure. Furthermore, this demasking strategy has been expanded to generate cyclotriphosphazene from a hexaazide precursor P_3N_{21} via a different stimulation method (photolysis) for complementary measurements by matrix isolation infrared and ultraviolet spectroscopy.

Introduction

"Seeing is believing"[1] is a very human trait even though we know that our visual impressions cannot be fully trusted. Still, also in the molecular world, the visualization of atoms and molecules has begun to revolutionize not only the way we perceive and characterize but also how we make molecular structures. On-surface synthesis (OSS) by single-molecule imaging and manipulation[2] has demonstrated its prowess recently with the preparation of, for instance, arynes,[3] triangulene,[4] and cyclo[18]carbon[5] with the goal of making unusual molecular structures. Here we demonstrate that even fleetingly existing, highly reactive inorganic structures not accessible by conventional means can be prepared through OSS. At the same time, we remark that the mechanisms of on-surface reactivity are not yet well understood and possibly quite different from traditional synthetic approaches.[6] It does, however, expand our arsenal of synthetic methods as we demonstrate with the synthesis of D_{3h}-symmetric cyclotriphosphazene (P_3N_3), an inorganic aromatic analogue of benzene.

Hückel aromaticity[7] is attributed to monocyclic, planar organic compounds with $4n+2$ conjugated π-electrons (n is a natural number including zero) with no bond length alternation featuring high chemical and structural stability: the classic example is benzene (**I**, C_6H_6, with six π-electrons, $n=1$, Figure 1a).[8] In contrast to the well-studied aromatic organic molecules, knowledge about prototypical aromatic inorganic molecules is not as abundant due to their

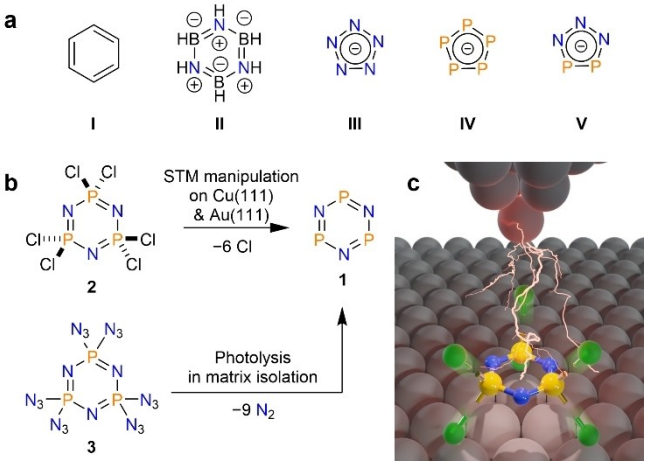

Figure 1. Synthetic approaches toward cyclotriphosphazene (P_3N_3 **1**). a) Structurally characterized prototypical organic and inorganic aromatic molecules. b) Reaction scheme for the generation of P_3N_3 **1** via STM tip-induced dechlorination of hexachlorophosphazene ($P_3N_3Cl_6$, **2**) on the Cu(111) and Au(111) surface or photo-induced extrusion of dinitrogen from hexaazidephosphazene (P_3N_{21}, **3**) under matrix isolation conditions. c) Illustration for the single-molecule dechlorination reaction of **2** triggered by applying voltage pulses with the STM tip. The atoms are color-coded: P (yellow), N (blue), Cl (green), and Cu (grey).

[*] Dr. Q. Zhong,[+] Dr. D. Ebeling, Prof. A. Schirmeisen
Institute of Applied Physics, Justus Liebig University Giessen, Giessen (Germany)
E-mail: schirmeisen@uni-giessen.de

Dr. Q. Zhong,[+] Dr. A. Mardyukov,[+] Dr. E. Solel,[+] Dr. D. Ebeling, Prof. A. Schirmeisen, Prof. P. R. Schreiner
Center for Materials Research (ZfM), Justus Liebig University Giessen, Giessen (Germany)
E-mail: prs@uni-giessen.de

Dr. A. Mardyukov,[+] Dr. E. Solel,[+] Prof. P. R. Schreiner
Institute of Organic Chemistry, Justus Liebig University Giessen, Giessen (Germany)

[+] These authors contributed equally to this work.

instability and lack of suitable synthetic methods.[9] Borazine (**II**, $B_3N_3H_6$) is referred to as inorganic benzene as it is isoelectronic;[10] however, it is not regarded as an aromatic molecule because of its limited electron delocalization.[11] There are also charged aromatic species such as anions N_5^- and P_5^- (**III** and **IV**)[12] and heteroatomic $P_2N_3^-$ (**V**),[13] which are valence isoelectronic to the prototypically aromatic $C_5H_5^-$ cyclopentadienyl anion. The aromatic nature of cyclotriphosphazene (**1**, P_3N_3, Figure 1b) is supported by nucleus-independent chemical shifts (NICS) computations.[14] The negative NICS value of −3.9 parts per million (ppm) at 1.0 Å above the plane of the ring for P_3N_3 **1** and −10.2 ppm for C_6H_6 **I** indicates that **1** is aromatic but much less than benzene.[15] Even though a homodesmotic evaluation also indicates that **1** captures only about one third of the aromatic stabilization of benzene, **1** has been computed as the most favorable structure among the many isomers that can be envisaged for P_3N_3.[16] Therefore, **1** as an inorganic analogue of benzene, is regarded as a benchmarking molecule of the inorganic Hückel aromatic system.

The pursuit of cyclotriphosphazene **1** has lasted for 45 years but still remains a great challenge in terms of both controlled synthesis and structural elucidation due to its high reactivity and fleeting existence.[15–17] Compound **1** was first prepared in 1977 through thermal decomposition of triphosphorus pentanitride (P_3N_5) and was characterized by its sparse infrared (IR) spectrum under matrix isolation conditions in krypton and argon;[17d] the infrared assignment is incomplete (see below) but further spectroscopic characterization attempts were unsuccessful. More recently, **1** and its high energy isomers were prepared through an entirely different approach, namely through ionizing phosphine (PH_3)-ammonia (NH_3) ices with hard radiation.[16,18] Its identification rests on isomer selective photoionization and mass spectrometry, which does not offer direct structural information. Therefore, the selective preparation of **1** is unresolved and relies, as we demonstrate here, on having a suitable precursor and a reliable synthetic method. At the same time, the planar D_{3h}-symmetric ring structure of **1** still awaits the definitive confirmation by real-space observation at the single-molecule level. A great advantage of OSS is that this highly reactive target molecule may be stabilized by adsorption on surface at low temperatures, which would enable high-resolution imaging of the molecular structure by scanning tunneling microscopy (STM) and atomic force microscopy (AFM), as done for pentacene,[19] benzene derivatives[20] and other organic aromatic molecules.[21]

Here we present a reliable method to generate **1** on Cu(111) and Au(111) surfaces at 5.2 K via voltage pulse-induced detachment of six chlorine substituents from the commercially available precursor hexachlorophosphazene ($P_3N_3Cl_6$, **2**) with the STM tip (Figure 1b,c). A series of STM and AFM images of the precursor, intermediates and product, as well as the dissociated Cl atoms, explicitly reveals a multi-step dechlorination of **2** and the generation of **1**. Despite being complex reactions, we have achieved a 91 % yield of **1** on Cu(111). The dissociated Cl atoms surrounding **1** were removed by vertical atom manipulation[22] to provide a clean isolated product. We demonstrate by means of atomic resolution AFM imaging using a CO functionalized tip that **1** indeed possesses D_{3h} symmetry. The regularly alternating P and N atoms are distinguishable by their different atomic radii, which is supported by DFT computations and AFM simulations. In line with the successful demasking strategy to synthesize **1** from its more stable derivatives, we also outline the selective synthesis of **1** in an argon matrix (10 K) via photolysis of an alternative precursor P_3N_{21} **3** (Figure 1b), allowing for complementary characterization by infrared and ultraviolet spectroscopy.

Results and Discussion

On-Surface Synthesis of P_3N_3 1 from 2

The adsorption structures of **2** were characterized by high-resolution imaging and DFT computations (Figures S1 and S2). To acquire pristine **1**, one "simply" needs to detach the Cl substituents from the P_3N_3 ring of **2** by thermal, electrical or light stimulation, with the hope that the ring structure stays intact in the dechlorination. Thermal dehalogenation is the most used reaction for efficient on-surface covalent assembly (polymerization)[23] toward diverse one- and two-dimensional carbon-based nanostructures, e.g., nanographenes and other carbon allotropes.[24] In contrast, intermolecular coupling should be avoided for the on-surface synthesis of single-molecule products, especially for reactive molecules. Actually, the thermal reactions of **2** on Cu(111) were found to preferentially provide complex non-planar clusters of random size and shapes (Figure S3). Alternatively, scanning probe manipulation has proven to be an effective tool to affect chemical reactions of single molecules, especially for dehalogenation reactions,[3,6,25] by applying local voltage pulses between the probe tip and the sample surface. More importantly, molecular diffusion is completely suppressed at 5.2 K, which enables reactive intermediates and products to be preserved and imaged.

We took advantage of the molecular manipulation technique to tackle the challenge of precisely scissoring the six P–Cl bonds of the ultra-small (diameter of about 6 Å) precursor **2**. Specifically, a simple procedure was designed to trigger the dechlorination of **2** on Cu(111): The STM tip is first positioned over the center of the target molecule (STM set point 500 mV and 2 pA); then the STM feedback is cut off and a short voltage pulse (2.5–4.5 V and 100 ms) is applied. Subsequently, a new STM image is taken to examine the structural changes of the molecule. The complete dechlorination of **2** occurs in multiple steps as illustrated in Figure 2a–f. Therefore, partially dechlorinated intermediates (e.g., $P_3N_3Cl_4$, $P_3N_3Cl_3$, $P_3N_3Cl_2$, $P_3N_3Cl_1$) were observed, among which $P_3N_3Cl_1$ is the most typical. The chemical identity of $P_3N_3Cl_1$ was confirmed by high-resolution imaging as all the five dissociated Cl atoms and one attached (protruding) Cl atom were clearly resolved (Figure S4). However, it is more difficult to unambiguously recognize the structures of the other intermediates based on the limited features captured in the STM/AFM images of

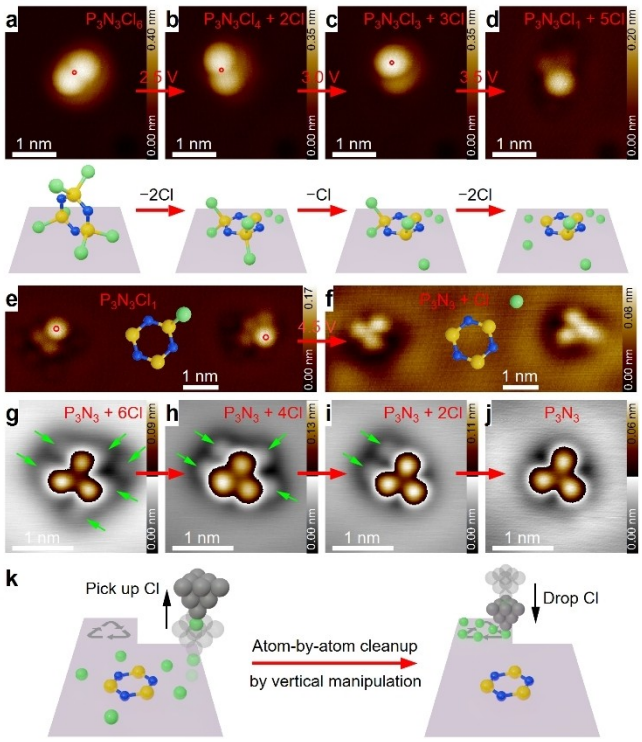

Figure 2. Tip-induced dechlorination of **2** on Cu(111). a)–d) A series of STM images and corresponding illustrative models showing the processes of tip-induced stepwise dechlorination of an individual molecule of **2**. The reactions were triggered by first positioning the metallic STM tip above the molecule (marked by red circles) with a set point of 500 mV and 2 pA, and then applying a short voltage pulse (2.5–3.5 V, 100 ms) with disabled tip-height feedback. e),f) STM images before and after triggering the last dechlorination of two $P_3N_3Cl_1$ intermediates by applying short voltage pulses of 4.5 V and 100 ms above the molecules (marked by red circles) with respect to a tunneling condition of 500 mV and 2 pA. The superimposed molecular models depict the chemical change. g)–j) A series of STM images demonstrating the atom-by-atom cleanup of the six dissociated Cl atoms (marked by green arrows) surrounding a molecule of **1**, via vertical manipulation as illustrated in (k). The image contrast was adjusted separately for the P_3N_3 molecule and the Cl atoms. The recycling symbol in (k) represents a clean area on Cu(111). Imaging parameters: (a–e) 500 mV, 2 pA; (f) 10 mV, 10 pA; (g) 10 mV, 100 pA; (h–j) 100 mV, 100 pA.

their highly three-dimensional geometries with dissociated Cl atoms hidden in close vicinity (Figure S5). DFT computations provide more insights into the adsorption structures of these partially dechlorinated intermediates (Figure S6) and the on-surface dechlorination reactions (Figure S7). Note that **2** on bilayer NaCl thin films, in contrast, just disappears in response to voltage pulses with no molecular fragments left in view, which is related to the high mobility of small molecules on NaCl surfaces.

The last dechlorination requires a much higher bias voltage than that for the other five Cl atoms (4.5 V vs 2.5–3.5 V), which is corroborated by the threshold voltages determined by tunneling current spectroscopy as a function of sample bias voltage (see details in Figure S5). Note that it requires further statistical analysis of the manipulation at different voltages to determine the exact thresholds for each dechlorination step,[26] which, however, is not the focus of this paper. In principle, it should be sufficient to realize complete elimination of the Cl atoms only with short and high voltage pulses of 4.5–5.0 V and 100 ms. We have experimented with the simplified procedure on 75 molecules of **2** and achieved a yield of 91% of **1** (Figure S8). The few failed cases presumably result from damage of the P_3N_3 ring (Figure S9). Interestingly, the effect of the high voltage pulses is often unlocalized, that is, the pulses are found to be able to trigger reactions of molecules 3.5–4.5 nm away where almost no tunneling current passes (Figure S10). This indicates that the P–Cl bond dissociation could also be induced by the high electric field close to the tip apex (on the order of 10^9 V/m)[27] or by indirect inelastic electron tunneling.[26,28]

The completion of sextuple dechlorination of a molecule of **2** is signified by the appearance of a three-fold symmetric molecular structure and six dissociated Cl atoms (Figures 2g and S11). However, the Cl atoms were closely adjacent to product **1** in most cases, which could interfere with its characterization. We therefore have performed a so-called "atom-by-atom cleanup", as illustrated in Figure 2k, to deliberately remove the Cl atoms by vertical atom manipulation.[22] The manipulation procedure includes three steps: (1) To pick up a Cl atom, the STM tip is first positioned at the target Cl atom and moved toward it by 0.3–0.4 nm with respect to the STM set point (typically 10 mV, 10 pA). (2) A new STM image is taken to check the success of pick-up. If not, step (1) will be repeated. (3) The Cl modified tip is poked into a clean area on the Cu(111) surface by 1.0–1.5 nm to get rid of the Cl atom and re-obtain a Cu tip. Figure 2g–j displays four key frames in the process of disposing the Cl atoms (marked by green arrows). This procedure is easily reproducible and is supported by another example in Figure S11. The separation of the Cl atoms from the P_3N_3 ring suggests that there is no chemical bonding between them.

Atomic-Level Characterization of 1 on Cu(111)

Product **1** was scrutinized in real space via high-resolution STM and AFM imaging and spectroscopy using a CO-functionalized tip. In the STM images (Figure 3a,b), the molecule was visualized as a three-fold symmetric star shape with three bright lobes evenly distributed around a dark center. High-resolution constant-current AFM images reveal another three smaller protrusions alternating with the three bigger lobes, forming a six-membered ring (Figure 3c). The three large and the three small bulges should correspond to the P and N atoms, respectively, considering their significantly different atomic radii (P: 2.142 Å, N: 1.921 Å, see Methods).

The geometry of the P_3N_3 ring was further characterized by constant-height AFM imaging. Bond-resolved AFM imaging of the planar ring structure was achieved by scanning at a close tip-sample distance (Figure 3e). The P_3N_3 ring is adsorbed parallel to the Cu(111) surface with the ring centered over a *hcp* hollow site and the three N atoms

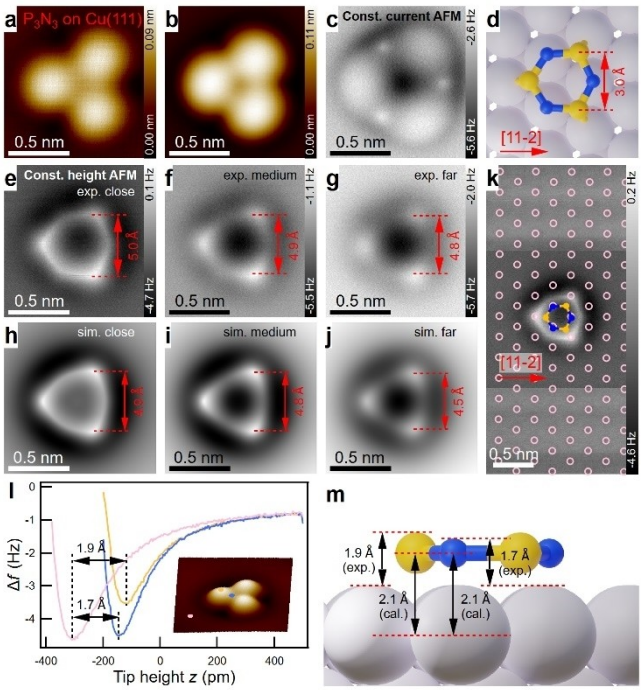

Figure 3. Real-space identification of **1** adsorbed on Cu(111). a) STM image of an individual molecule of **1**. b), c) Constant-current STM and AFM images simultaneously recorded with a CO-functionalized tip. d) Top view of the DFT computed adsorption structure of **1** on Cu(111). e)–g) Constant-height AFM images of the molecule recorded at different tip heights. h)–j) Corresponding simulated AFM images using a neutral CO tip with a lateral stiffness $k = 0.20\ \mathrm{N\,m^{-1}}$. k) Varied-height AFM image with atomic resolution of both the molecule and the adjacent Cu(111) surface. A Cu(111) lattice and a molecular model of **1** were fitted to the image; color-code: P (yellow), N (blue), and Cu (pink). l) Spectra of frequency shift as a function of tip height $\Delta f(z)$. The spectra were taken at the positions marked in the inset by dots of the corresponding colors. m) Side view of **1** on Cu(111) annotated with experimentally measured and computed adsorption heights of the P and N atoms. Imaging parameters: (a) 100 mV, 10 pA; (b, c) 10 mV, 100 pA; Tip height offset $\Delta z = -200$ pm (e), −180 pm (f), −160 pm (g), and −370/−200 pm for the imaging of Cu(111) surface and the P_3N_3 molecule in (k), relative to 100 mV, 10 pA.

pinned to the adjacent top sites (Figure 3d,k). Note that the P atoms always appear brighter (higher) than the N atoms at varied tip-surface distances (Figure 3e–g). The adsorption heights were measured to be approximately 1.7 Å (N) and 1.9 Å (P) by frequency shift spectroscopy as a function of tip height ($\Delta f(z)$, Figure 3l), while DFT computations reveal a perfectly planar adsorption structure of **1** with a height of 2.1 Å for both P and N. Note that the experimental and computed heights correspond to top-to-top and center-to-center distances (Figure 3m), respectively. The measured height difference (approximately 20 pm) between P and N is of similar order as their difference in atomic radii (22 pm). The planar D_{3h}-symmetric ring structure of **1** is a clear evidence of the aromatic form of P_3N_3 in contrast to other nonplanar and nonaromatic isomers.[16] The aromaticity of **1** is even enhanced by its adsorption on metal surfaces according to NICS and current density analysis (Figures S12 and S13).

To obtain a better understanding of the submolecular contrast we performed AFM image simulations using the mechanical probe particle model.[29] In the AFM simulations, a 2D tip-sample force map is generated via raster scanning of the DFT computed adsorption geometry of **1** on Cu(111) (Figure 3d, including the Cu surface) by a flexible probe particle at constant height, which is further converted into a frequency shift AFM image. Figure 3h–j shows the simulated AFM images of **1** at different tip-sample distances. The simulated AFM images reproduce the features in the experimental AFM images regarding the symmetry, shape, overall size, and the relative brightness of P and N atoms. There are some slight discrepancies, e.g., the different darkness in the center of the P_3N_3 ring in Figure 3e vs 3h, which should be ascribed to the simplified modeling of the sample and the tip as stated below.

The qualitative consistency between AFM simulations and experiments is achieved by carefully considering the different atomic radii of P and N and the tip-sample electrostatic interaction. The so-called bond-level AFM contrast is known to mainly arise from the Pauli repulsion[19] and short-range electrostatic interaction.[30] The hetero-elemental ring of **1** exhibits heterogeneous charge distribution in the gas phase (P: +1.95 e; N: −1.95 e) due to significant interatomic charge transfer according to the Bader charge analysis.[31] For the surface-adsorbed **1**, DFT computations reveal that the P and N atoms have an uneven charge distribution (P: +1.57 e; N: −1.97 e), leading to a total charge transfer (−1.20 e) from the Cu(111) surface to the molecule. Accordingly, the atomic radii of the P and N in surface-adsorbed **1** were recalculated with their charges taken into account as previously reported in other cases of ionic systems.[32] In the AFM simulations, the CO tip apex (O atom) is assigned with a point charge ranging from −0.10 e to +0.10 e, and the point charges of P and N atoms are incorporated as well. The varied tip charge causes significant changes in the AFM contrast (Figure S14). Here, a neutral CO tip provides the best match with the experimental AFM images (Figure 3e–j), although previous studies have indicated that the CO tip carries a small negative charge (e.g., −0.05 e) in front of the terminal O atom.[30c,e] This needs to be further evaluated by more refined DFT-based AFM simulations.[30b]

It is worth noting that pristine **1** is a closed-shell singlet molecule due to the variable valency of phosphorous (valency of 3 and 5 in the product **1** and the precursor **2**, respectively). Despite the charge transfer, the P_3N_3 on Cu(111) is still in a closed-shell singlet state and this electronic configuration is stable according to the computations. If the surface-adsorbed **1** were a radical anion, it would have been an open-shell singlet and the symmetry of the adsorption structure would have been broken, which is not the case here. In fact, the charges on P_3N_3 do not mean that there is a transfer of a complete electron to the molecule. There is instead transfer of partial electron densities (in equal amounts for two opposite spin-sign electrons, not just one of them) from the metal to the

molecule. The charge transfer should be responsible for the depression around the molecule of **1** in the STM images (Figure 3a, b) as an effect of charge screening.[33]

In quantitative terms, the main discrepancy between the AFM images and the expected molecular structure is a significantly increased apparent bond length. The measured P–P distance is 5.0 Å at the tip height where the optimal contrast is obtained (Figure 3e), while the computed P–P distance is 3.0 Å. However, the expanded apparent P–P distance in the experiment is corroborated by the AFM simulations (4.9 Å, Figure 3h). This overestimation of the molecular size is known to originate from forced tilting of the CO tip at the periphery of the imaged molecule. In the case of AFM images of a hexagon of C_{60} that were measured with CO tips an enlargement of the same order has been observed.[34] The size of **1** in the simulated AFM images increases with decreasing lateral stiffness of the CO tip (Figure S15). A spring constant k of 0.20 $N\,m^{-1}$ leads to the best agreement with the experiments (Figure 3e–g vs 3h–j), which is close to the experimentally measured k value of 0.24 $N\,m^{-1}$ for a Cu-based CO tip.[35]

Generation and Characterization of 1 on Au(111)

To minimize the possible influence of molecule-surface interactions on the structure of **1**, we reproduced the synthesis and imaging of **1** on Au(111). In addition to NaCl films and Xe films,[3–4,36] Au(111) is also significantly less reactive than Cu(111), thus it has been widely adopted for the OSS of many highly reactive nanostructures, such as open-shell nanographenes.[37] Product **1** was generated on Au(111) from precursor **2** through a series of STM manipulations similar to the procedure on Cu(111). Dissociated Cl atoms were often observed in the vicinity of the product (Figure 4a).

High-resolution STM and AFM imaging and DFT computations reveal the planar D_{3h}-symmetric ring structure of **1** (Figure 4b–g), which is comparable to the results on Cu(111). However, there is no obvious depression in the close vicinity of **1** in the STM images on Au(111) in comparison with that on Cu(111) (Figure 3a, b vs Figure 4a, b), which suggests a reduced charging of **1** on Au(111). DFT computations reveal that the charge distribution on the P and N atoms (P: +1.80 e; N: −1.90 e) is only slightly affected by the adsorption, leading to a much smaller total charge transfer (−0.30 e) from the Au(111) surface to the adsorbed **1**. Moreover, the adsorption height of **1** on Au(111) is larger than on Cu(111) with a measured difference of 10 pm and a computed difference of 20 pm (Figures 4h, i vs 3l, m), indicating weaker molecule-surface interactions on Au(111). The results on Au(111) should imply that physisorbed **1** would also be stable at the low temperature (5.2 K) we used.

Note that we also obtained a nonplanar adsorption structure of the P_3N_3 ring on Au(111) (Figure S16). The nonplanar P_3N_3 is different from all the known isomers of P_3N_3. It therefore represents a special surface-stabilized isomer of **1** with broken aromaticity. Detailed analysis of the

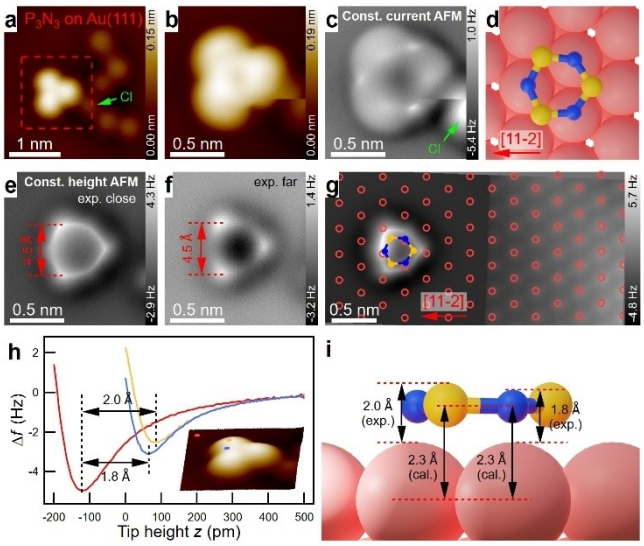

Figure 4. Real-space identification of **1** adsorbed on Au(111). a) STM image of an individual molecule of **1**. b), c) Constant-current STM and AFM images simultaneously recorded with a CO-functionalized tip. d) Top view of the DFT computed adsorption structure of **1** on Au(111). e), f) Constant-height AFM images of the molecule recorded at different tip heights. g) Varied-height AFM image with atomic resolution of both the molecule and the adjacent Au(111) surface. A Au(111) lattice and a molecular model of **1** were fitted to the image; color-code: P (yellow), N (blue), and Au (red). h) Spectra of frequency shift as a function of tip height $\Delta f(z)$. The spectra were taken at the positions marked in the inset by dots of the corresponding colors. i) Side view of **1** on Au(111) annotated with experimentally measured and computed adsorption heights of the P and N atoms. Imaging parameters: (a) 100 mV, 5 pA; (b, c) 10 mV, 100 pA; Tip height offset $\Delta z = -130$ pm (e), −100 pm (f), and −320/−140 pm for the imaging of Au(111) surface and the P_3N_3 molecule in (g), relative to 100 mV, 10 pA.

adsorption structure and properties of the nonplanar P_3N_3 is an ongoing subject of studies in our laboratory. Reversible switching between the nonplanar P_3N_3 and planar **1** could be realized by voltage pulses (0.5 to 3.5 V, Figures S17–S19). Especially, the structural change of **1** usually occurs at low bias voltages (typically 0.5 V). The metastability of **1** on Au(111) however prevents further characterization of its electronic properties by scanning tunneling spectroscopy considering its large gas phase HOMO-LUMO gap (3.89 eV, computed at B3LYP/6-311G(3df,3pd)).

Matrix Isolation Spectroscopy

The OSS and direct visualization of **1** has undoubtedly demonstrated the reliability of our synthetic strategy, i.e., releasing reactive **1** ring from its precursor by removing the chlorine atoms. To solidify our findings additionally and characterize **1** also spectroscopically, we sought to adapt our synthesis to matrix isolation techniques. Matrix isolation spectroscopy is a practical approach for the characterization (e.g., infrared and UV/Visible spectroscopy) of highly reactive molecules via their isolation in noble gas matrices at low temperatures.[38] These conditions help suppress isomer-

ization to thermodynamically more stable isomers and aggregation.

The photolysis of matrix-isolated precursors is the technique most frequently used for the synthesis of reactive species.[39] However, the photolysis of **2** fails to provide the expected unsubstituted **1** because in a solid argon matrix the dissociated Cl atoms are confined at the initial position relative to the P_3N_3 ring where recombination between the P and Cl atoms occurs spontaneously. Therefore, the challenge is to design and prepare a suitable precursor that can generate inert and unreactive byproducts.

The thermally and photochemically induced elimination of dinitrogen (N_2) from suitable azide precursors has proven to be a reliable method for the synthesis of reactive species. For example, it was shown recently that phosphonic azides can be readily triggered thermally and photochemically to release N_2 and leave behind highly reactive phosphorus species.[40] With this idea in mind, we hypothesized that the known hexaazidephosphazene (**3**)[41] would be an ideal precursor for the clean synthesis of **1** through the elimination of nine N_2 molecules (Scheme S1).

Precursor **3** was prepared following the protocol of Klapötke and colleagues[41] (for synthetic details see the Supporting Information). We aimed at recording the complete IR spectrum of **1** in an argon matrix to demonstrate that **3** is an ideal starting material yielding **1** cleanly. Matrices containing **3** were obtained by slow deposition of **3** from a storage bulb at room temperature with a large excess of argon on the surface of the matrix window held at 10 K. The IR spectrum of **3** isolated in solid argon matrices is characterized by intense absorption bands centered at 2153 cm^{-1}; this compares well with the most intense absorption of **3** at 2162 cm^{-1}.[41] Irradiation ($\lambda = 254$ nm) of matrices containing **3** results in the rapid and complete vanishing of its IR signals and simultaneous appearance of new prominent IR bands at 1137 and 718 cm^{-1} (Figure 5a). The 1137 cm^{-1} band agrees excellently with the single band reported for **1** earlier[17d] and with our unscaled B3LYP/6-311++G(3df,3pd) computations (Table S1). Most importantly, no other IR bands are present that would correspond to partially decomposed diazides and tetraazides, nitrene intermediates or other isomers of **1** (like the Dewar-form),[16] and the formation of **1** is essentially quantitative. The light-induced conversion of **3** into **1**, in principle, should also work on metal or more inert surfaces. However, thermal treatment and STM manipulation by voltage pulses on the Cu(111) surface failed to accomplish this complex reaction to yield **1** or its oligomers (Figures S20–S26). The challenges of demasking **3** by STM manipulation should be independent of the substrates, e.g., less reactive Au(111).

The UV/Vis spectrum of argon matrix-isolated **3** has its absorption maximum at 197 nm (Figure 5b), in good agreement with its computed UV/Vis spectrum using time-dependent density functional theory (TD-DFT). In accordance with the IR experiments, the photolysis of **3** results in a decrease of the band at 197 nm, which is accompanied by a growth of signals at 225, 289, and 422 nm (Figure 5b). The photolysis product of **3** can readily be assigned to **1** on the basis of the good correlation of the experimentally observed

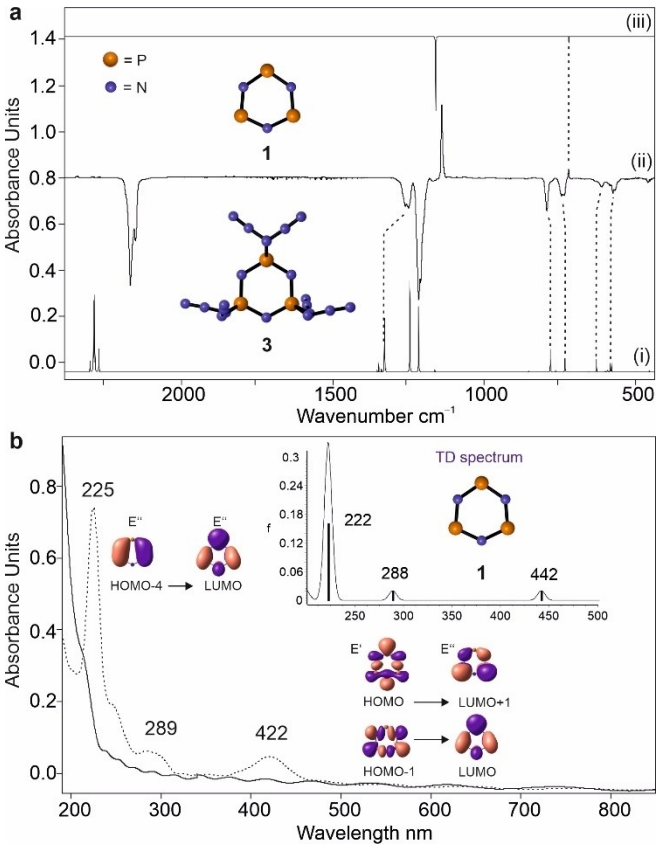

Figure 5. Photochemistry of P_3N_{21} **3** and spectroscopic measurements under matrix isolation conditions. a) i) IR spectrum of **3** computed at B3LYP/6-311++G(3df,3pd) (unscaled). ii) IR difference spectra showing the photochemistry of **3** after irradiation at $\lambda = 254$ nm in argon at 10 K. Downward bands assigned to **3** disappear while upward bands assigned to **1** appear after 20 min irradiation time. iii) IR spectrum of **1** computed at B3LYP/6-311++G(3df,3pd) (unscaled). b) Solid: UV/Vis spectrum of **3** isolated at 10 K in Ar. Dashed: UV/Vis spectrum of **1** at 10 K; the photochemistry of **3** after irradiation at $\lambda = 254$ nm in Ar at 10 K. Inset: Computed UV/Vis spectrum of **1** at TD-B3LYP/6-311++G(3df,3pd).

transitions with the electronic excitations at 222 nm ($f = 0.16$), 288 nm ($f = 0.02$), and 442 nm ($f = 0.02$) computed at TD-B3LYP/6-311++G(3df,3pd). Inspection of the molecular orbitals of **1** reveals that the strong transition at 225 nm corresponds to a $\pi \rightarrow \pi^*$ transition while the band in the visible region at 422 nm originates from an $n \rightarrow \pi^*$ excitation.

Hence, the proper choice of precursor structure is key to the generation of new molecular entities. As we demonstrate here, the starting material needs to be optimally adapted to the method of identification. Nevertheless, the photolytic synthesis in matrix isolation and the on-surface synthesis are closely related and support each other based on the following three reasons. First, the two precursors $P_3N_3Cl_6$ (**2**) and P_3N_{21} (**3**) used in this work are comparable in the sense that they both have a P_3N_3 core protected by six masking groups. Second, the common synthetic route is to remove the masking groups with external stimuli. We have tried all the four combinations of the two precursors and two stimuli (UV light and STM manipulation) and found two successful

combinations, i.e., **2** by STM manipulation and **3** by UV light. Third, the chemical identities of the P_3N_3 products in both systems are essentially the same (Table S2) despite the molecule-surface charge transfer. The charge transfer on Au(111) is even negligible. The matrix experiment substantiates demasking of more stable derivatives of P_3N_3 as an effective synthetic strategy toward **1** and provides complementary insights into the properties of **1** by IR and UV/Vis spectroscopy. We point out that the *in situ* photolytic synthesis of **1** from **3** under the scanning probe microscope is still an interesting topic for future investigations, which requires a different experimental setup to directly introduce UV light to the sample surface in the microscope. The convergence of independent preparation methods for the generation of fleetingly existing molecules and the confluence with quantum mechanical computations additionally solidifies their identification and characterization.

Conclusion

Scanning probe manipulation and microscopic imaging, in combination with proper choice of precursors, enabled a reliable on-surface synthesis route to produce and characterize a fleetingly existing molecule, namely cyclotriphosphazene **1**, an inorganic analogue of benzene. By selectively breaking six out of twelve bonds of a very small ($\approx$6 Å) precursor $P_3N_3Cl_6$ (**2**) toward the unsubstituted **1**, we demonstrate the great potential of STM manipulation in realizing unprecedentedly delicate fabrication of elusive molecules. The molecular structure of **1** has been visually resolved as a planar D_{3h}-symmetric six-membered ring by atomic-resolution AFM imaging in real space, which is underpinned by AFM simulations. In light of the feasibility of generating **1** from its more stable derivatives, we also photochemically synthesized **1** from an alternative precursor, P_3N_{21} **3**, under matrix isolation conditions and characterized **1** by IR and UV/Vis spectroscopy. Density functional theory computations support the experimental interpretation of the structure as a 6π aromatic species with a singlet ground state. To the best of our knowledge, our results represent the first case of OSS of an inorganic aromatic molecule. We expect that the OSS strategies presented in this work can be applied to the preparation and visualization of many other reactive species as well.

Acknowledgements

The authors thank Felix Keul for the preparation of **3**. Financial support by the LOEWE Program of Excellence of the Federal State of Hesse (LOEWE Focus Group PriOSS "Principles of On-Surface Synthesis") is gratefully acknowledged. Further funding was provided by the Deutsche Forschungsgemeinschaft via grants SCHI 619/13, EB 535/1-1, EB 535/4-1 and MA 8773/3-1. Open Access funding enabled and organized by Projekt DEAL.

Conflict of Interest

The authors declare no conflict of interest.

Data Availability Statement

The data that support the findings of this study are available in the supplementary material of this article.

Keywords: Atomic Force Microscopy · Matrix Isolation · Photochemistry · Reactive Intermediates · On-Surface Synthesis

[1] T. Fuller, *Gnomologia Adagies and Proverbs; Wise Sentences and Witty Sayings, Ancient and Modern, Foreign and British*, B. Barker and A. Bettesworth and C. Hitch, London, **1732**, p. 174.
[2] S. W. Hla, L. Bartels, G. Meyer, K. H. Rieder, *Phys. Rev. Lett.* **2000**, *85*, 2777–2780.
[3] N. Pavliček, B. Schuler, S. Collazos, N. Moll, D. Pérez, E. Guitián, G. Meyer, D. Peña, L. Gross, *Nat. Chem.* **2015**, *7*, 623–628.
[4] N. Pavliček, A. Mistry, Z. Majzik, N. Moll, G. Meyer, D. J. Fox, L. Gross, *Nat. Nanotechnol.* **2017**, *12*, 308–311.
[5] K. Kaiser, L. M. Scriven, F. Schulz, P. Gawel, L. Gross, H. L. Anderson, *Science* **2019**, *365*, 1299–1301.
[6] Q. Zhong, A. Ihle, S. Ahles, H. A. Wegner, A. Schirmeisen, D. Ebeling, *Nat. Chem.* **2021**, *13*, 1133–1139.
[7] E. Hückel, *Z. Phys.* **1931**, *70*, 204–286.
[8] a) T. M. Krygowski, M. K. Cyrański, *Chem. Rev.* **2001**, *101*, 1385–1420; b) P. v. R. Schleyer, *Chem. Rev.* **2001**, *101*, 1115–1118; c) P. v. R. Schleyer, H. Jiao, *Pure Appl. Chem.* **1996**, *68*, 209–218; d) M. Solà, *WIREs Comput. Mol. Sci.* **2019**, *9*, e1404.
[9] a) L. Nyulászi, *Chem. Rev.* **2001**, *101*, 1229–1246; b) A. R. Eulenstein, Y. J. Franzke, N. Lichtenberger, R. J. Wilson, H. L. Deubner, F. Kraus, R. Clérac, F. Weigend, S. Dehnen, *Nat. Chem.* **2021**, *13*, 149–155.
[10] A. Stock, E. Pohland, *Ber. Dtsch. Chem. Ges. B* **1926**, *59B*, 2215–2223.
[11] B. Kiran, A. K. Phukan, E. D. Jemmis, *Inorg. Chem.* **2001**, *40*, 3615–3618.
[12] a) M. Baudler, S. Akpapoglou, D. Ouzounis, F. Wasgestian, B. Meinigke, H. Budzikiewicz, H. Münster, *Angew. Chem. Int. Ed.* **1988**, *27*, 280–281; b) A. Vij, J. G. Pavlovich, W. W. Wilson, V. Vij, K. O. Christe, *Angew. Chem. Int. Ed.* **2002**, *41*, 3051–3054.
[13] A. Velian, C. C. Cummins, *Science* **2015**, *348*, 1001–1004.
[14] P. v. R. Schleyer, C. Maerker, A. Dransfeld, H. Jiao, N. J. R. van Eikema Hommes, *J. Am. Chem. Soc.* **1996**, *118*, 6317–6318.
[15] a) A. A. Starikova, N. M. Boldyreva, R. M. Minyaev, A. I. Boldyrev, V. I. Minkin, *ACS Omega* **2018**, *3*, 286–291; b) E. Elguero, I. Alkorta, J. Elguero, *Heteroat. Chem.* **2018**, *29*, e21441.
[16] C. Zhu, A. K. Eckhardt, A. Bergantini, S. K. Singh, P. R. Schreiner, R. I. Kaiser, *Sci. Adv.* **2020**, *6*, eaba6934.
[17] a) R. Ahlrichs, M. Bär, H. S. Plitt, H. Schnöckel, *Chem. Phys. Lett.* **1989**, *161*, 179–184; b) J. O. Jensen, *J. Mol. Struct.* **2005**, *729*, 229–234; c) G. Sánchez-Sanz, *Tetrahedron* **2015**, *71*, 826–839; d) R. M. Atkins, P. L. Timms, *Spectrochim. Acta Part A* **1977**, *33A*, 853.
[18] C. Zhu, A. K. Eckhardt, S. Chandra, A. M. Turner, P. R. Schreiner, R. I. Kaiser, *Nat. Commun.* **2021**, *12*, 5467.
[19] L. Gross, F. Mohn, N. Moll, P. Liljeroth, G. Meyer, *Science* **2009**, *325*, 1110–1114.

[20] Z. M. Han, G. Czap, C. L. Chiang, C. Xu, P. J. Wagner, X. Y. Wei, Y. X. Zhang, R. Q. Wu, W. Ho, *Science* **2017**, *358*, 206–210.
[21] Q. Zhong, X. Li, H. Zhang, L. Chi, *Surf. Sci. Rep.* **2020**, *75*, 100509.
[22] L. Bartels, G. Meyer, K. H. Rieder, *Appl. Phys. Lett.* **1997**, *71*, 213–215.
[23] L. Grill, M. Dyer, L. Lafferentz, M. Persson, M. V. Peters, S. Hecht, *Nat. Nanotechnol.* **2007**, *2*, 687–691.
[24] a) J. M. Cai, P. Ruffieux, R. Jaafar, M. Bieri, T. Braun, S. Blankenburg, M. Muoth, A. P. Seitsonen, M. Saleh, X. L. Feng, K. Müllen, R. Fasel, *Nature* **2010**, *466*, 470–473; b) Q. Fan, L. Yan, M. W. Tripp, O. Krejčí, S. Dimosthenous, S. R. Kachel, M. Chen, A. S. Foster, U. Koert, P. Liljeroth, J. M. Gottfried, *Science* **2021**, *372*, 852–856; c) Q. Fan, D. Martin-Jimenez, D. Ebeling, C. K. Krug, L. Brechmann, C. Kohlmeyer, G. Hilt, W. Hieringer, A. Schirmeisen, J. M. Gottfried, *J. Am. Chem. Soc.* **2019**, *141*, 17713–17720.
[25] D. Ebeling, Q. Zhong, T. Schlöder, J. Tschakert, P. Henkel, S. Ahles, L. Chi, D. Mollenhauer, H. A. Wegner, A. Schirmeisen, *ACS Nano* **2019**, *13*, 324–336.
[26] H. Gawronski, J. Carrasco, A. Michaelides, K. Morgenstern, *Phys. Rev. Lett.* **2008**, *101*, 136102.
[27] B. Borca, T. Michnowicz, R. Petuya, M. Pristl, V. Schendel, I. Pentegov, U. Kraft, H. Klauk, P. Wahl, R. Gutzler, A. Arnau, U. Schlickum, K. Kern, *ACS Nano* **2017**, *11*, 4703–4709.
[28] P. A. Sloan, S. Sakulsermsuk, R. E. Palmer, *Phys. Rev. Lett.* **2010**, *105*, 048301.
[29] P. Hapala, G. Kichin, C. Wagner, F. S. Tautz, R. Temirov, P. Jelínek, *Phys. Rev. B* **2014**, *90*, 085421.
[30] a) P. Hapala, M. Švec, O. Stetsovych, N. J. van der Heijden, M. Ondráček, J. van der Lit, P. Mutombo, I. Swart, P. Jelínek, *Nat. Commun.* **2016**, *7*, 11560; b) M. Ellner, P. Pou, R. Pérez, *ACS Nano* **2019**, *13*, 786–795; c) J. van der Lit, F. Di Cicco, P. Hapala, P. Jelínek, I. Swart, *Phys. Rev. Lett.* **2016**, *116*, 096102; d) P. Zahl, Y. Zhang, *Energy Fuels* **2019**, *33*, 4775–4780; e) M. Ellner, N. Pavliček, P. Pou, B. Schuler, N. Moll, G. Meyer, L. Gross, R. Pérez, *Nano Lett.* **2016**, *16*, 1974–1980.
[31] G. Henkelman, A. Arnaldsson, H. Jónsson, *Comput. Mater. Sci.* **2006**, *36*, 354–360.
[32] a) J. B. Peng, J. Guo, P. Hapala, D. Y. Cao, R. Z. Ma, B. W. Cheng, L. M. Xu, M. Ondracek, P. Jelinek, E. G. Wang, Y. Jiang, *Nat. Commun.* **2018**, *9*, 122; b) A. Liebig, P. Hapala, A. J. Weymouth, F. J. Giessibl, *Sci. Rep.* **2020**, *10*, 14104.
[33] J. Mieres-Perez, K. Lucht, I. Trosien, W. Sander, E. Sanchez-Garcia, K. Morgenstern, *J. Am. Chem. Soc.* **2021**, *143*, 4653–4660.
[34] L. Gross, F. Mohn, N. Moll, B. Schuler, A. Criado, E. Guitián, D. Peña, A. Gourdon, G. Meyer, *Science* **2012**, *337*, 1326–1329.
[35] A. J. Weymouth, T. Hofmann, F. J. Giessibl, *Science* **2014**, *343*, 1120–1122.
[36] a) N. Pavliček, P. Gawel, D. R. Kohn, Z. Majzik, Y. Y. Xiong, G. Meyer, H. L. Anderson, L. Gross, *Nat. Chem.* **2018**, *10*, 853–858; b) Z. Majzik, A. B. Cuenca, N. Pavliček, N. Miralles, G. Meyer, L. Gross, E. Fernández, *ACS Nano* **2016**, *10*, 5340–5345.
[37] a) S. Mishra, D. Beyer, K. Eimre, S. Kezilebieke, R. Berger, O. Gröning, C. A. Pignedoli, K. Müllen, P. Liljeroth, P. Ruffieux, X. Feng, R. Fasel, *Nat. Nanotechnol.* **2020**, *15*, 22–28; b) S. Mishra, G. Catarina, F. Wu, R. Ortiz, D. Jacob, K. Eimre, J. Ma, C. A. Pignedoli, X. Feng, P. Ruffieux, J. Fernández-Rossier, R. Fasel, *Nature* **2021**, *598*, 287–292.
[38] a) V. E. Bondybey, A. M. Smith, J. Agreiter, *Chem. Rev.* **1996**, *96*, 2113–2134; b) A. Mardyukov, W. Sander, in *Encyclopedia of Radicals in Chemistry, Biology and Materials*, (Eds.: C. Chatgilialoglu, A. Studer) John Wiley & Sons Ltd. **2012**, pp 207–228.
[39] a) R. Mondal, C. Tönshoff, D. Khon, D. C. Neckers, H. F. Bettinger, *J. Am. Chem. Soc.* **2009**, *131*, 14281–14289; b) C. M. Nunes, S. N. Knezz, I. Reva, R. Fausto, R. J. McMahon, *J. Am. Chem. Soc.* **2016**, *138*, 15287–15290; c) S. V. Chapyshev, E. Mendez-Vega, W. Sander, *Chem. Eur. J.* **2021**, *27*, 1258–1269.
[40] a) X. Chu, Y. Yang, B. Lu, Z. Wu, W. Qian, C. Song, X. Xu, M. Abe, X. Zeng, *J. Am. Chem. Soc.* **2018**, *140*, 13604–13608; b) X. Zhao, X. Chu, G. Rauhut, C. Chen, C. Song, B. Lu, X. Zeng, *Angew. Chem. Int. Ed.* **2019**, *58*, 12164–12169; c) A. Mardyukov, F. Keul, P. R. Schreiner, *Angew. Chem. Int. Ed.* **2020**, *59*, 12445–12449; d) W. Qian, R. C. Wende, P. R. Schreiner, A. Mardyukov, *Angew. Chem. Int. Ed.* **2023**, *62*, e202300761.
[41] M. Göbel, K. Karaghiosoff, T. M. Klapötke, *Angew. Chem. Int. Ed.* **2006**, *45*, 6037–6040.

Manuscript received: July 16, 2023
Accepted manuscript online: September 13, 2023
Version of record online: October 12, 2023